Friedrich-Alexander-Universität
Naturwissenschaftliche Fakultät

Bachelor Thesis
in Physics

Efficient Evaluation of the Performance of Neutrino Telescope Geometries

---

Elena Meier

Supervisor: Prof. Dr. Claudio Kopper

Erlangen Centre for Astroparticle Physics

Submission date: 21 August 2025

Abstract

Over the last decade, many important discoveries have been made in the field of high-energy neutrino astronomy. The IceCube Neutrino Observatory identified two possible point sources of neutrino emission and a diffuse neutrino flux from the Galactic plane. However, the statistics and the field of view of IceCube are limited. Therefore, new neutrino telescopes at different locations are currently in planning or under construction. In order to maximize the capabilities of a single detector, the detector geometry must be optimized for the observation target in the planning phase. This is usually done with time- and computationally expensive Monte Carlo simulations. With this method, only a few detector geometries can be tested.

Therefore, in this thesis, first steps were taken in implementing a faster approach, which tries to approximate some steps, usually done in Monte Carlo simulations, analytically.

Contents

1 Introduction

One of the main goals of astroparticle physics is to determine the origin and sources of ultra high energetic cosmic rays (UHECRs) to better understand the most energetic events in the universe. Besides UHECRs, also neutrinos are assumed to be produced at these sources. Because they only interact weakly, they do not get deflected and are rarely absorbed. Hence, neutrinos are suitable particles for tracing back their origin [1]. However, due to their small cross section it is difficult to gain enough statistics for clear detections.

Over the last decade, many discoveries were made in neutrino astronomy. The IceCube Neutrino Observatory found evidence for two point sources (NGC 1068 [2] and TXS 0506+056 [3]) and also for a diffuse neutrino flux from the Galactic Plane [4]. However, none of these source-discoveries yet achieved a background-only hypothesis rejection of 5σ. Additionally, these are only very few sources. Therefore, efforts are made to improve the detection rate. Better results can be achieved by combining the field of view of several existing detectors around the world, like in the PLEnuM framework [5], and by optimizing the detector geometry for specific observation targets for future telescopes.

The goal of this thesis is to investigate the impact of different detector geometries on the detection significance when performing a diffuse-astrophysical-flux and a point source analysis.
To determine the detection significance, a binned Poisson likelihood test using Asimov data [6] is used.
For the comparison of different geometries, the detector response, which consists of the angular and energy resolution and effective area of these detectors, needs to be modeled. This is usually done in computationally expensive Monte Carlo simulations [7]. In this thesis, a less computationally expensive approach will be introduced, by calculating the effective area, which is an important parameter for the computation of the significance, based on neutrino, muon and detector properties.

2 Neutrinos

In this section, neutrinos and their role in astronomy and astroparticle physics are introduced.

2.1 Neutrino properties

Neutrinos (ν_e, ν_μ, ν_τ, $\overline{\nu}_e$, $\overline{\nu}_\mu$, $\overline{\nu}_\tau$) are standard-model-particles that belong to the group of fermions due to their spin of $\frac{1}{2}$. There, they are part of the leptons, the particles of which matter is composed of [1]. They only interact via the weak force, i.e. via the exchange of a $\mathrm{W}^{\pm}$ or Z^0 boson and, hence, have no electrical or color charge [8].

In the standard model they are assumed to be massless. However, due to the discovery of neutrino oscillations, it is known that the mass eigenstates have a non-zero rest mass. This mass is very small, the current upper limit is 0.45 eV, set by the KATRIN experiment [8].

Besides their low mass, also their cross section and therefore interaction probability is very low compared to electromagnetically or strongly interacting particles [1].

2.2 Neutrino astronomy

2.2.1 Production

Because UHECRs, e.g. relativistic protons, are measured, the existence of astrophysical high-energetic neutrinos was assumed and also confirmed in 2013 by the IceCube Neutrino Observatory [9]. Cosmic rays interact in the environment of their source and produce secondary particles, like pions, which can decay into neutrinos. The secondary particles can also decay into high energetic photons, which is why it is expected that neutrino and gamma ray emission correlate and that their spectra are similar.

One possible decay chain for the production of neutrinos is:

$$\pi^+ \rightarrow \mu^+ \nu_\mu \quad \text{and afterwards:} \quad \mu^+ \rightarrow e^+ \nu_e \overline{\nu}_\mu \, .$$

The production of gamma rays can happen via:

$$\pi^0 \rightarrow \gamma\gamma \, .$$

Therefore, cosmic rays, gamma rays and neutrinos are closely related [1].

2.2.2 Importance for astronomy

For studying the sources of these particles, the observation of neutrinos has some advantages compared to the observation of cosmic rays and gamma rays. High energy photons can be absorbed inside their source or on the way to Earth and cosmic rays can get deflected due to their electric charge [1]. In contrast, as already mentioned in subsection 2.1, neutrinos have a very small cross section and only interact weakly. Hence, absorption is very unlikely and they do not get deflected by interstellar magnetic fields. Consequently, neutrinos propagate in a straight line from their source to earth and are therefore suited for determining the location of their sources. However, their low cross section also makes them difficult to detect. This is why large-volume detectors (see section 3) are needed [10].

2.2.3 Flux components

The flux of high-energy neutrinos detected at Earth consists of the atmospheric neutrino flux, the diffuse astrophysical flux and the point source astrophysical flux [1].

Atmospheric neutrino flux

Atmospheric neutrinos are produced in interactions of cosmic rays with the atmosphere and are considered as background when trying to detect astrophysical neutrinos. There are two types: standard and prompt neutrinos. Standard atmospheric neutrinos are produced in decays of charged pions and kaons, whereas prompt neutrinos stem from weak decays of mesons or baryons made of heavy quarks [1].

Diffuse astrophysical flux

The diffuse astrophysical flux is produced when cosmic rays interact with gas inside or outside the Milky Way. In 2013, the IceCube Collaboration reported the detection of an astrophysical diffuse neutrino flux [9] and in 2023 the "Observation of high-energy neutrinos from the Galactic plane" [2].

Point source astrophysical flux

It is assumed that most extragalactic point sources cannot be resolved spatially and therefore contribute to the detected isotropic, diffuse flux. This flux is distinguished from the atmospheric background by its harder spectrum [1]. Source candidates are active galactic nuclei (AGNs), supernova remnants (SNRs), pulsar wind nebula (PWNs), gamma-ray bursts (GRBs) or tidal disruption events (TDEs) [2] [11]. TXS 0506+056 [3] and NGC 1068 [2], both AGNs, were identified as potential sources by the IceCube Neutrino Telescope.

3 Water and Ice Cherenkov Detectors

In this thesis, a less computationally expensive approach for detector design optimization is developed. Therefore, this section gives an introduction about the general setup of water and ice Cherenkov telescopes.

3.1 Instrumentation

Due to the low interaction probability of neutrinos, as described in section 2, detectors with a large volume are needed for neutrino detection. Detectors of this size can only be built in natural environments [10]. In optically transparent media, like water or glacial ice, the Cherenkov effect (see subsection 3.2) can be exploited for the detection of neutrinos. Current and future detectors consist of vertical cable strings deployed several kilometers inside glacial ice or below sea level. Digital optical modules (DOMs) that detect Cherenkov photons are attached to these strings. Already operating detectors have a volume of around 1 km^3 and a number of strings of around 100. Some future detectors are planned to have a volume of up to 30 km^3 and a few thousand strings [12].

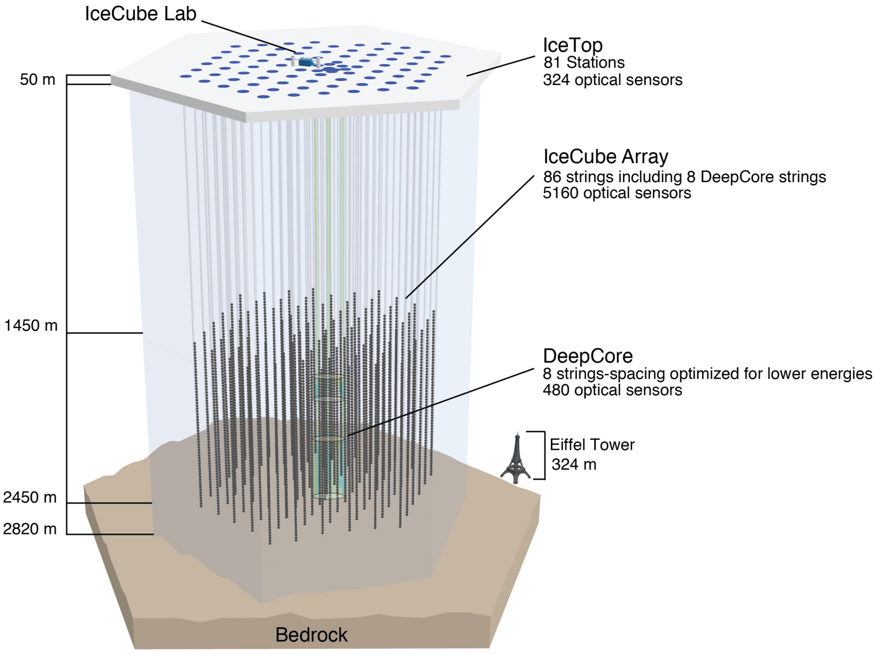

Figure 3.1: The IceCube Neutrino Observatory as an example for an ice Cherenkov neutrino telescope. Image taken from [13].

Currently operated water/ice Cherenkov neutrino telescopes are the IceCube Neutrino Observatory [13], located near the geographical south pole, KM3NeT-ARCA and -ORCA [14], located in the Mediterranean Sea and Baikal-GVD located in lake Baikal [15].

Since the work in this thesis often refers to properties of IceCube, this detector is described in more detail (cf. Figure 3.1).

The in-ice component consists of an array of 86 strings in a hexagonal grid. A total number of 5160 DOMs is attached to this grid. The instrumented volume of 1 km^3 is located in a depth between 1450 m and 2450 m. On each string there are 60 DOMs with a separation of 17 m. The strings have a distance from each other of around 125 m. Neutrinos with an energy in the range of TeV to PeV can be measured with this detector geometry design [13]. DeepCore is a more densely instrumented part of the in-ice component. Therefore, neutrinos with an energy of 10 GeV to 100 GeV can be measured there [13].

3.2 Cherenkov effect

Neutrinos cannot be observed directly, which is why indirect methods like the Cherenkov effect are used. When neutrinos interact with the nucleons in water or ice, charged secondary particles are produced, which travel through the medium at a speed faster than the phase velocity of light in this medium. These secondary particles cause polarization along their path in the medium and Cherenkov radiation is emitted as a cone of light [16]. This radiation is detected at the photomultiplier tubes (PMTs) in the DOMs of the detector. Depending on the particle's velocity and the medium's properties, the angle of this cone varies. For particles at the speed of light, the cone has an angle of 42° in water and of 41° in ice. Depending on the type of interaction, different event signatures can be observed in the detector [10].

3.3 Event signatures

Since high-energy neutrino telescopes are sensitive to neutrinos of about 10 GeV (e.g. IceCube DeepCore) and above [13], deep-inelastic-scattering processes are the dominant interaction type. Therefore, neutrino-nucleon interactions can either happen through a charged current (CC) or neutral current (NC) interaction, so the detector is sensitive to every flavor [1]. In CC interactions a neutrino with a certain flavor l interacts with a nucleon N, a W-boson is exchanged, and the respective charged lepton and a hadronic shower X are produced (from [1]):

$$\nu_l(\overline{\nu}_l) + N \rightarrow l^-(l^+) + X \,.$$

In NC interactions, a neutrino with a certain flavor interacts with a nucleon, a Z-boson is exchanged, and a neutrino with the same flavor and a hadronic shower are produced (from [1]):

$$\nu_l(\overline{\nu}_l) + N \rightarrow \nu_l(\overline{\nu}_l) + X \,.$$

A visualization of these interactions is shown in Figure 3.2.

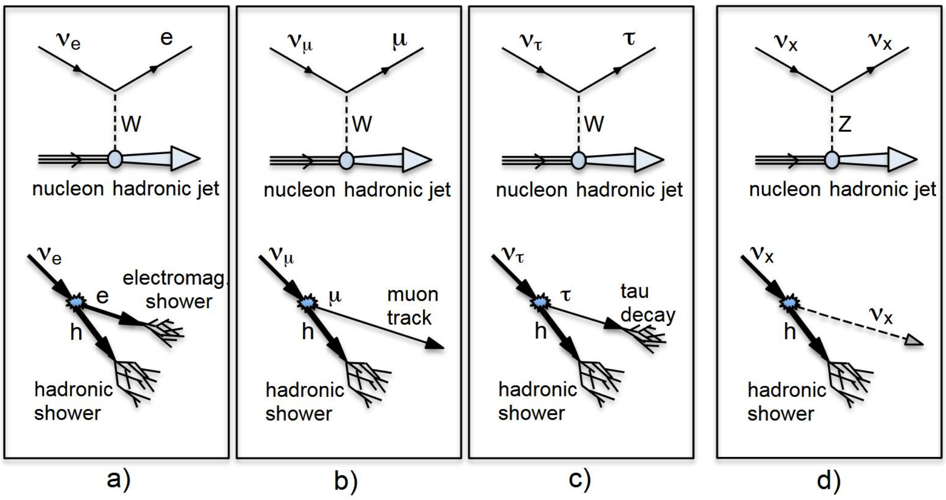

Figure 3.2: Interaction diagrams and event signatures of neutrino-nucleon interactions. Images a), b) and c) show the CC interaction types, image d) shows the NC interaction types. Image taken from [10].

There are two main event topologies observed in the detector: One is the shower/cascade-like event (Figure 3.2 a), d)), which occurs due to CC interactions of electron-neutrinos or NC interactions of neutrinos of any flavor. The other type is the track-like event (Figure 3.2 b)) that is produced in CC interactions of muon-neutrinos [1]. CC interactions of tau-neutrinos can have various different signatures (Figure 3.2 c)), because of the different tau-lepton decay channels [7]. In this thesis, only track-like events are considered.

4 Detector response modeling

The goal of this thesis is to investigate the impact of different detector geometries on the detection significance that results from a point source or a diffuse-flux analysis. To be able to compare different geometries, the detector response, which consists of the resolution and effective area of the tested detector geometries, needs to be modeled. In this thesis, the effective area is calculated based on neutrino-, muon- and detector properties.
In this section, the calculation of the effective area for an ideal detector through an already existing code [17] and the implementation of a detection efficiency in this calculation is described.

4.1 Effective area calculation

The effective area is a very important quantity of a telescope because it represents the area of a hypothetical telescope, which would detect every neutrino passing through it. It is energy and declination dependent. Furthermore, it usually much smaller than the surface area of the detector because of the low interaction probability of neutrinos [10].
For an idealized detector that detects every muon produced in an interaction taking place on the detector surface, the neutrino effective area is calculated as [17]:

$$A_{\text{eff}}(\theta, E, r, h) = P_{\text{trans}}(\theta, E) \cdot P_{\text{int}}(\theta, E, r, h) \cdot A_{\text{proj}}(\theta, r, h) \cdot \varepsilon(\theta, E, r, h)\,, \qquad (4.1)$$

where

- θ is the zenith angle,
- E is the neutrino energy,
- r and h are the radius and height of a cylindrical detector,
- P_{trans} is the transmission probability, which is the probability for a neutrino reaching the detector without interacting (see Figure 4.1),
- P_{int} is the interaction probability, which is the probability for a neutrino interacting in (or near) the detector volume,
- A_{proj} is the projected area of the detector, which is the area of the detector "seen" by an incoming neutrino,
- ε is the detection efficiency. It is a number between 0 and 1, where 1 describes the idealized detector that detects every muon. The implementation of a more realistic detector is described in subsection 4.2.

For the calculation of the transmission probability, tables with precomputed values and interpolations in between are used.

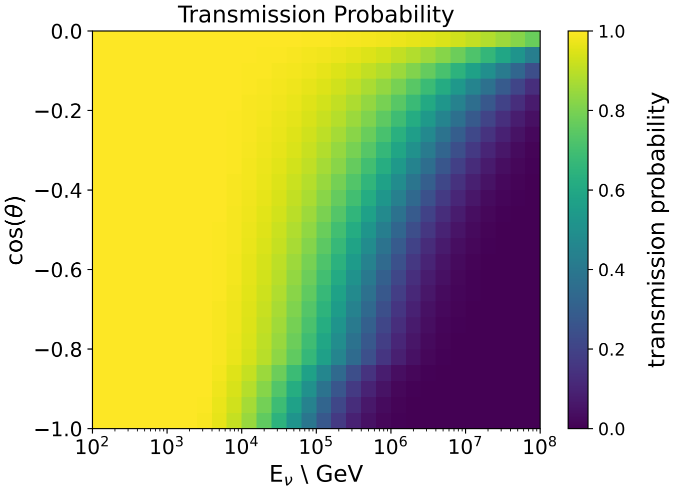

Figure 4.1: Visualization of the transmission probability P_{trans}. The higher the energy and the closer to $\cos(\theta) = -1$, the smaller the transmission probability due to earth absorption.

The projected area consists of the projected top and side surface, which depend on the angle of the incoming neutrino.
The interaction probability is calculated by [17]:

$$P_{\text{int}} = 1 - e^{-n \cdot \sigma_\nu(E) \cdot L} \,. \tag{4.2}$$

Here, the total neutrino-nucleon cross section, σ_ν, is needed. It is energy and interaction-type dependent (CC, NC, ν, $\overline{\nu}$) and is obtained from precomputed tables and interpolation. Additionally, the average chord length, L, for a given direction must be considered. It describes the average distance a neutrino can travel inside the detector volume. The larger the chord length, the higher the interaction probability. Since only muon-neutrinos and therefore muon tracks are considered in this thesis, the chord length must be extended by a variable that takes into account that muon-neutrinos can also be detected when interacting outside the detector volume. The nucleon density of water, n, is also needed in the formula.

Examples of detection efficiency matrices with $\varepsilon = 1$ and $\varepsilon \in [0, 1]$ are shown in Figure 4.7.

4.2 Detection efficiency implementation

In subsection 4.1 the effective area for an idealized fully, instrumented detector that would detect every muon passing through is calculated. However, in reality, detectors consist of optical modules that have a certain distance from each other, as described in subsection 3.1. As a result, events inside a detector are not always identified as an event, since photons produced by a muon may not reach any optical module or do not meet the requirements for a detection. Additionally, the hardware itself has a certain efficiency. To account for these limitations, a modeled detection efficiency is introduced in the following.

The modeling is done by simulating a number of muons, which cause a yield of photons at the optical modules inside a modeled detector. Filter thresholds are modeled according to IceCube's muon effective area since it is connected to the detection efficiency. The detection efficiency is given by the number of events that passed the filters divided by all generated muons.

Light yield at an optical module

For the implementation of the detection efficiency, an analytical approximation for the light emission of a muon, so called "lightsaber" muons, is used [7] [18]. There, muon tracks are assumed to have an infinite length and uniformly emit a constant number of photons per meter, which is obtained from the averaged light emission of stochastic muons [7]. For short distances it is also assumed that there is almost no scattering, so the photons travel in a straight line towards the optical modules. For larger distances scattering is considered. These are the two limiting cases in Equation 4.3.

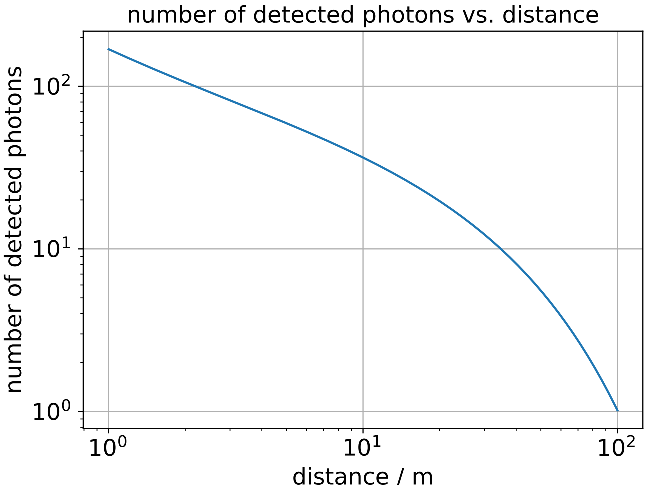

Figure 4.2: Plot of Equation 4.3 for a muon-energy of 1 TeV.
The formula shows the number of photons detected at a DOM with respect to the distance of the muon track from the DOM.

The light yield at one optical module is dependent on the energy of the muon and the distance of the muon track from the optical module and is obtained from an empirical formula, which is visualized in Figure 4.2, (from [18]):

$$\mu(r) = l_0 A \cdot \frac{1}{2\pi \sin\theta_c} e^{-r/\lambda_p} \cdot \frac{1}{\sqrt{\lambda_\mu r} \tanh\left(\sqrt{r/\lambda_\mu}\right)}, \tag{4.3}$$

$$\text{where} \quad \sqrt{\lambda_\mu} = \frac{\lambda_c}{\sin\theta_c}\sqrt{\frac{2}{\pi\lambda_p}} \quad , \quad \lambda_p = \sqrt{\frac{\lambda_a \lambda_e}{3}} \quad , \quad \lambda_c = \frac{\lambda_e}{3\zeta} \quad \text{and} \quad \zeta = \exp\left(-\frac{\lambda_e}{\lambda_a}\right),$$

and

- r is the distance of the muon track to the DOM,
- l_0 is the number of photons per meter,
- A is the effective photon collection area of the optical module,
- θ_c is the Cherenkov angle,
- λ_p is the propagation length in ice,
- λ_a is the averaged absorption length in ice,
- λ_e is the averaged effective scattering length in ice.

Parametrization of a muon track

A muon track can be parametrized as a straight line in $\mathbb{R}^3$, since it is assumed to have an infinite length:

$$\vec{g}(r) = \vec{p} + r \cdot \vec{u}\,. \tag{4.4}$$

where $\vec{p}$ is the point on the line and $\vec{u}$ is the direction vector. $\vec{p}$ and $\vec{u}$ are produced randomly and uniformly on a cylinder surface. This cylinder has the height and radius of the detector geometry considered.

Parametrization of detector geometries

In the previous sections expressions for the light yield at an optical module and the muon track are introduced. To be now able to compute the distance between the DOM and the muon track, the positions of the DOMs must be initialized.

Three detector geometries are used: the positions of the DOMs in IceCube (Figure 4.3 a)), a cylindrical shaped detector (Figure 4.3 b)) and a detector with the shape of a sunflower (Figure 4.3 c)).

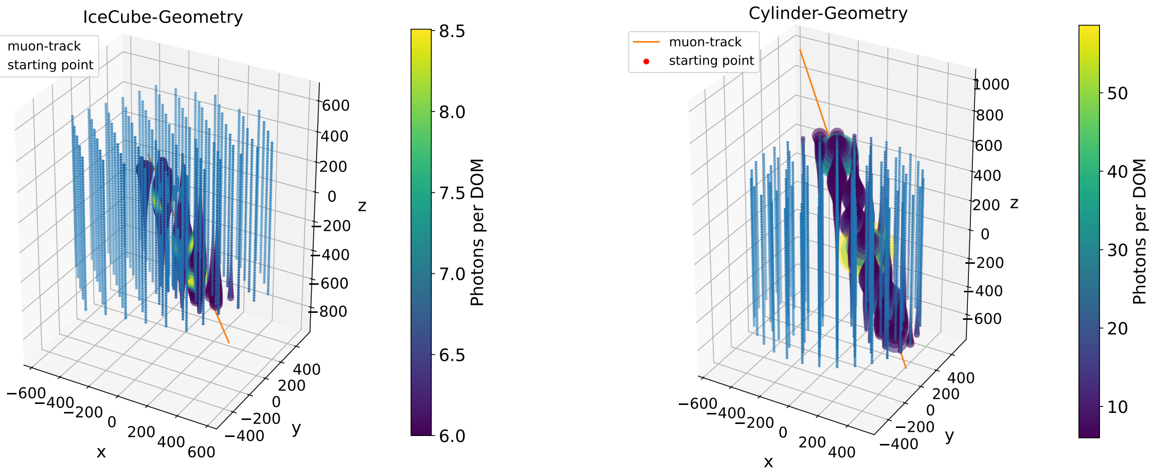

(a) IceCube **(b)** Cylinder

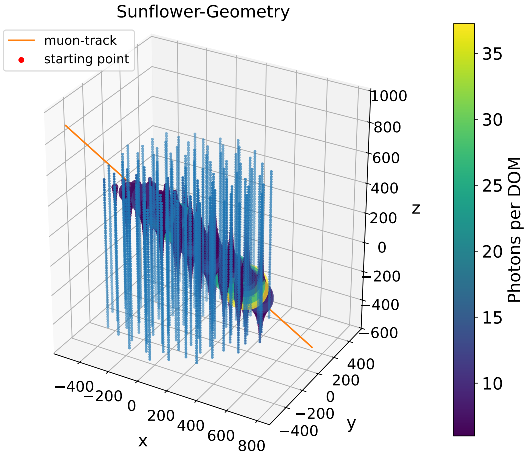

(c) Sunflower

Figure 4.3: Visualization of a muon track (orange line) with an energy of 1 TeV in IceCube, a cylindrical detector and a "sunflower" detector. The more photons a DOM detected the larger the dot and the brighter the color. DOMs that detected less than six photons are depicted as a blue dot.

For the IceCube detector, a file with already existing DOM positions from the ToyCube-simulation [19], is used. It consists of 86 strings and 60 DOMs per string, has a radius of about 500 m and a height of 1000 m.

The cylindrical detector is parametrized similarly to the IceCube detector with $i \cdot 6$ strings per concentric ring, with i being the number of the concentric ring counted from the inside to the outside, and one single string in the middle of the detector. In Figure 4.3 b) the detector has 91 strings with 60 DOMs per string and also a radius of 500 m and a height of 1000 m. These values can be varied for comparing the detection significances of different geometries later.

The sunflower geometry is parametrized as in [20] as:

$$r = s\sqrt{n}\,, \quad \phi = \frac{2\pi}{g^2}n\,, \tag{4.5}$$

where $g = \frac{1+\sqrt{5}}{2}$ is the golden ratio. n is a parameter for the string position, since the larger n is, the further away is the string from the center. It has the length of the number of strings implemented. s is the spacing parameter. The detector shown in Figure 4.3 c) also has 91 strings with 60 DOMs each and a radius of roughly 500 m and a height of 1000 m.

Distance calculations

With the parametrization of the muon track and the detector geometry, the distance between the muon track and the optical module, which is needed for the calculation of the light yield in Equation 4.3, are computed. This is done using the approximation that the photons travel in a straight line from the source, which is the parametrized muon track, to the optical modules:

$$d = \frac{|\overrightarrow{pa} \times \vec{u}|}{|\vec{u}|}\,, \tag{4.6}$$

where d is the shortest distance between track and DOM, $\vec{p}$ is the point on the line, $\vec{u}$ is the direction vector, $\vec{a}$ the position of an optical module and $\overrightarrow{pa} = \vec{a} - \vec{p}$.

Detection efficiency

The detection efficiency is defined as:

$$\varepsilon = \frac{\text{number of muon-track events that passed the filter}}{\text{total number of muon-track events}} \in [0, 1]\,. \tag{4.7}$$

Therefore, filters that model the actual triggering and event reconstruction processes in IceCube, need to be introduced.

For the calculation of ε a number of muons coming from random directions and being distributed uniformly, is produced by parameterizing a number of muon tracks as straight lines that pass through the detector. They are or are not counted as event, depending on the filter-thresholds set.

First, a photon-threshold, which defines the minimum number of photons that must arrive at an optical module, is implemented. This is then used to define a second filter, the DOM-threshold, which is the minimum number of optical modules that detects at least the number of photons of the photon-threshold. As a third filter, the distance-threshold is introduced. There, the travel-distance of a muon inside the detector must be larger than the value of this threshold. It is applied on the events that passed the previous two filters.

For the calculation of the traveled distance of the muon in the detector, the foot of the perpendicular, F, from the optical module to the muon track is calculated. This is done by using that the dot product of two orthogonal vectors is zero. The formula obtained is the formula for an orthogonal projection of a point on a straight line:

$$F = \vec{p} + ((\vec{a} - \vec{p}) \cdot \vec{u})\vec{u}\,. \tag{4.8}$$

All distances between these feet of the perpendiculars are calculated and the largest distance out of those is compared with the distance threshold and used for obtaining the detection efficiency.

The detection efficiency ε is dependent on the energy and direction of the muon.

Finding reasonable values for the thresholds

For obtaining realistic values for the detection efficiency, reasonable filter-thresholds must be chosen. The muon effective area is directly related to the detection efficiency, since it describes "how well" muons are detected and requires that the neutrino interacted with a nucleon.

Therefore, the modeled IceCube detector is used to determine the thresholds from the muon effective area of IceCube. The shape of the curve of the modeled detection efficiency (Figure 4.4 a)) should be similar to the curve of the muon effective area of IceCube obtained from [16]. For adjusting the shape of the detection efficiency curve it was multiplied by the highest value of the muon effective area from [16] for each angular range which corresponds to 100 percent. With this, the detection efficiency (Figure 4.4 a)) is converted to a muon effective area (Figure 4.4 b)). Afterwards, the values of the filter thresholds were varied, such that the shape of the modeled and scaled detection efficiencies look similar to the muon effective areas of [16].

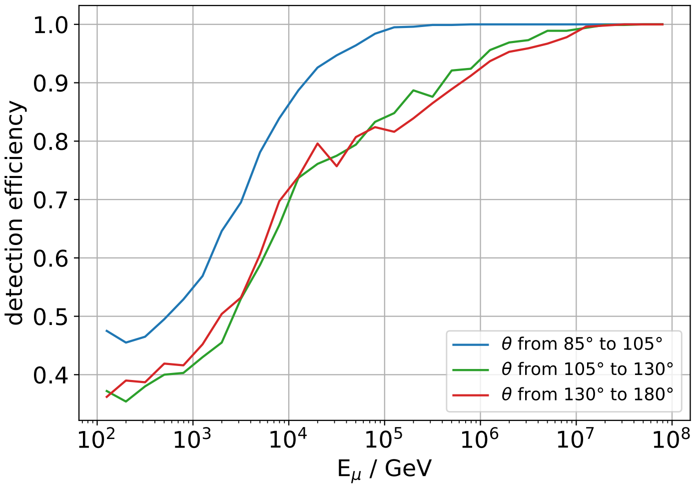

(a) Detection efficiency over muon-energy for three angular ranges depicted as blue, red and green curves.

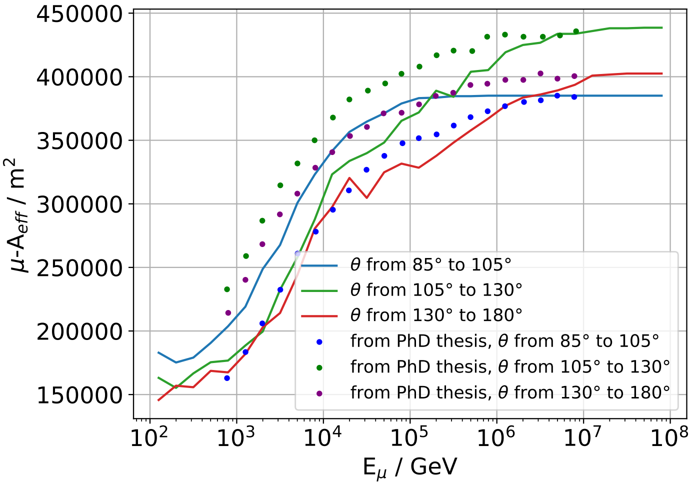

(b) Detection efficiencies multiplied by highest values of muon effective area plot from PhD thesis [16].

Figure 4.4: Detection efficiency and muon effective area plots for the modeled IceCube detector with 1000 generated muons, photon-threshold = 6, DOM-threshold = 30 and distance-threshold = 550 m.

The similar looking curve shapes in Figure 4.4 b) were achieved by setting the photon-threshold to 6, the DOM-threshold to 30 and the distance-threshold to 550 m. These values are used in the following for the analyses with the cylinder- and sunflower-detector-geometries.

Another way for converting the detection efficiency in a muon effective area was performed by calculation [17]:

$$A_{\mathrm{eff}_\mu} = \frac{\varepsilon \cdot \mathcal{A}}{2\pi \cdot (cos(\theta_2) - cos(\theta_1))}\,, \tag{4.9}$$

where ε are the detection efficiencies over the energies for the considered angular range

$(cos(\theta_2) - cos(\theta_1))$ (cf. Figure 4.4 a)) and $2\pi \cdot (cos(\theta_2) - cos(\theta_1))$ is the solid angle Ω. $\mathcal{A}$ is the acceptance, i.e. the projected area integrated over the angular range, of a cylinder with the same size of the detector.

However, this method yielded values for the muon effective area that are up to a factor 3 larger than the values from [16]. The reason for this discrepancy could not be determined and can be investigated in the future.

Because the muon effective area is only used to adjust the shape of the detection efficiency curves and is not needed in subsequent steps, this discrepancy between the two methods has no influence on the further analysis. Therefore, the previous scaling method with the values from [16] was used for adjusting the shapes of the curves and determining the filter thresholds.

Even though the filter-thresholds were set empirically, as described above, they are physically reasonable. In Figure 4.5 histograms depicting the distribution of counts for the three correlated filters are shown.

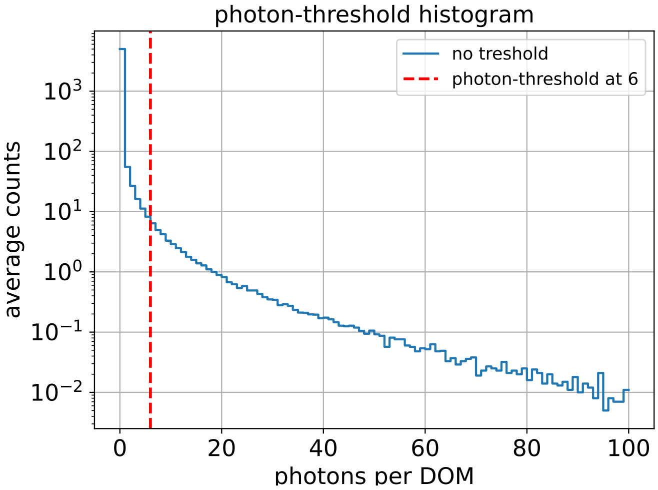

(a) photon-threshold

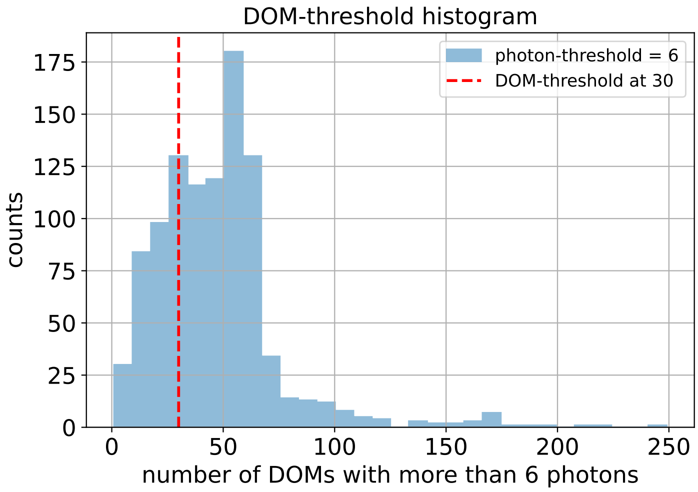

(b) DOM-threshold

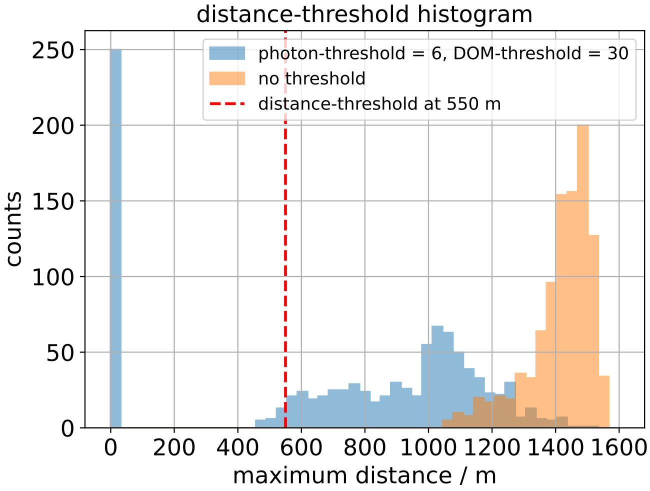

(c) distance-threshold

Figure 4.5: Filter-threshold histograms for the photon-threshold, DOM-threshold and distance-threshold with 1000 produced muons at an energy of 10 TeV. Note that the bar at the x-value 0 with 250 counts is an underflow bin produced by the code. When the number of DOMs that detect more than six photons does not pass the DOM-threshold of 30, the projected distances are set to -1 to make sure that they do not pass the distance-threshold.

In Figure 4.5 a), the number of DOMs that detected a certain number of photons is shown. The number of photons that is detected by a DOM is averaged over the number of muons used for producing this plot, which is 1000 in this case. This needs to be done because one muon leads to a detection of a number of photons at each DOM in the detector, hence for 1000 it needs to be averaged. The number of DOMs that detected more than six photons is obtained by calculating the area under the curve on the right side of the red threshold line. When doing this, it can be seen that only about 50 out of 5160 optical modules detect more than six photons.

In the actual IceCube detector, it is likely that six photons are sufficient for a detection, since IceCube DOMs are in principle able to detect single photons [13]. Because of existing dark noise, however, a single photon would not be enough since a certain number of them must be cut. In addition, the calculation of the photon yield of a DOM (Equation 4.3) already accounts for the loss of photons during the detection, because the effective photon collection area, A, is implemented. Therefore, a filter criterion of one optical module detecting at least six photons is reasonable or maybe even a bit conservative.

In Figure 4.5 b) the histogram for the DOM-threshold, with the photon-threshold being set, is shown. Most counts are around a number of 50 DOMs that detect more than six photons. Hence, a filter-threshold at 30 is reasonable since not too much and not too less events are cut with the DOM-threshold.

In Figure 4.5 c) the correlation between the thresholds can be seen. When plotting the distribution of counts over the largest on the muon track projected distance of optical modules, denoted as "maximum distance", without setting any threshold, the smallest length is already larger than 1000 m and gets as long as the whole detector. The reason for this is that in the implemented model detecting less than one photon is possible and therefore optical modules far away from the muon track are still considered in the calculation of the maximal distance. When setting the photon and the DOM-threshold the optical modules detecting a very small number of photons are cut and the on the muon track projected distance reaches values smaller than the threshold.

The threshold of 550 m is reasonable, because also here, not too much and not too less should be cut, and 550 m being about half of the height and diameter of the detector is a good length. In addition, in the real IceCube detector, long tracks are better for direction reconstruction than shorter ones.

Using the detection efficiency in the analysis

In the binned likelihood analyses and in the calculation of the effective area of the idealized detector, the effective area is a matrix with 30 energy-bins in x-direction and 25 $\cos(\theta)$- or $\sin(\delta)$-bins in y-direction. Since the detection efficiency scales the effective area, the two matrices must be multiplied. Therefore, a detection efficiency matrix with the same dimensions as the effective area matrix needs to be calculated. A visualization of them can be seen in Figure 4.6.

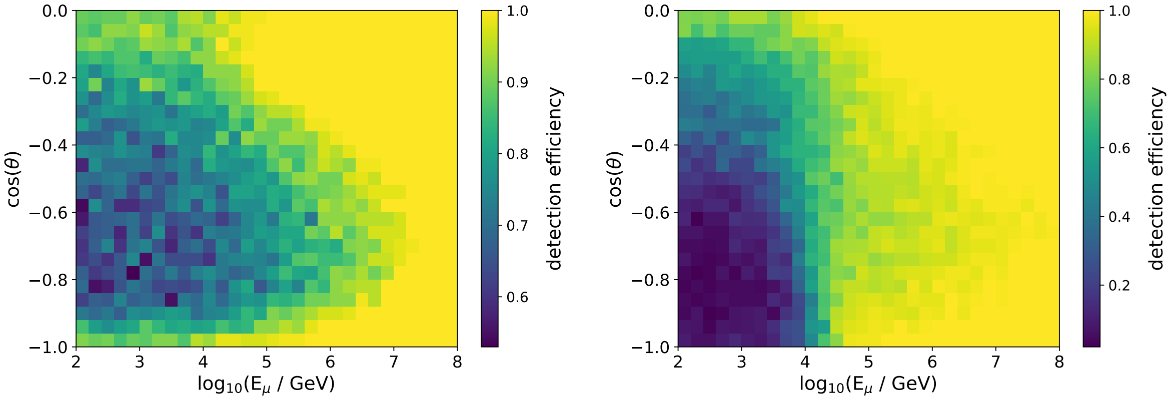

(a) detector radius = 500 m

(b) detector radius = 2000 m

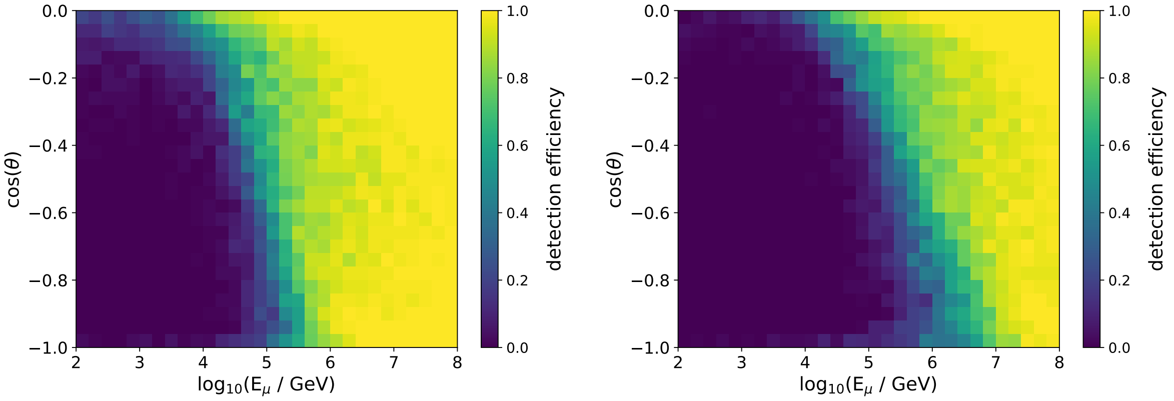

(c) detector radius = 4000 m

(d) detector radius = 6000 m

Figure 4.6: Visualization of the detection efficiency matrices calculated with the chosen filter-thresholds for a cylindrical detector with 469 strings, 60 DOMs per string and different radii.

In Figure 4.7 an effective area matrix of an ideal detector, as described in subsection 4.1, and an effective area matrix multiplied with the detection efficiency matrix in Figure 4.6 c) are shown.

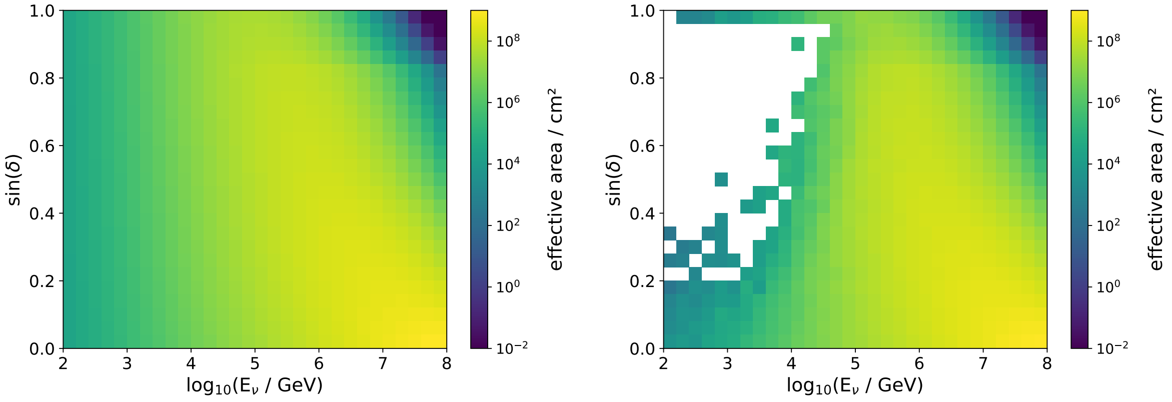

(a) effective area matrix multiplied by a detection efficiency of 1.

(b) effective area matrix multiplied by the detection efficiency matrix in Figure 4.6 c).

Figure 4.7: Visualization of the effective area matrices for an ideal detector and a detector with detection efficiency $\varepsilon \in [0, 1]$, both with a radius of 4000 m. The bounds of the color bar were set to obtain the same coloring in both plots for better comparison. At the geographic South Pole, $sin(\delta) = -cos(\theta)$ holds.

5 Binned Likelihood Analysis in the PLEnuM Framework

To compare different detector geometries a binned Poisson maximum likelihood analysis with Asimov data is performed [6]. The aim is to calculate a significance for each tested geometry at which the background hypothesis for a neutrino flux is rejected. The obtained significances are used to determine which detector geometry is best suited for detecting a specific flux component.

The general proceeding for performing such an analysis is the same for both the diffuse-flux and the point source analysis. First, the expected event rates are calculated based on flux models that have free fit parameters. Afterwards, the likelihood function is maximized to obtain the best-fit values. Next, a hypothesis test comparing the signal and background hypotheses is performed. Lastly, the significance with which the null hypothesis can be rejected is calculated.

5.1 Detector resolution

For calculating the expected event rates in subsubsection 5.3.2 the resolution of the detector needs to be known, since not the true event distribution is measured, but a smeared one.

The detector resolution for the diffuse flux is given by the energy resolution function, which is binned and used as smearing matrix. It describes the correlation between the reconstructed muon energy and the true neutrino energy. For the flux of the point source an energy resolution function and an angular resolution function are used [5]. No angular resolution function is needed for the diffuse flux, since it is assumed to be isotropically distributed. The resolution functions are obtained from the 10-year IceCube data release, [21], and adjusted to the binning used here [6].

5.2 Flux models

The total neutrino flux consists of the atmospheric neutrino flux, the background, and the astrophysical neutrino flux, the signal. The background is modeled with MCEq (Matrix Cascade Equation), where the free model parameter is ϕ_0^{atm}. The signal flux is assumed to follow a single power law:

$$\frac{d\phi_\nu}{dE_\nu} = \phi_0 \cdot \left(\frac{E_\nu}{E_0}\right)^{-\gamma} , \tag{5.1}$$

where E_ν is the neutrino energy, E_0 the energy normalization, ϕ_0 is the flux normalization and γ the spectral index. ϕ_0^{ast} and γ are the free fit parameters here.

In the Asimov data set, the model parameters, $\vec{\theta}_{true}$, for the used astrophysical diffuse flux are: $\phi_0 = 1.0 \cdot 10^{-18}$ GeV^{-1} cm^{-2} s^{-1} sr^{-1}, $E_0 = 100$ TeV and $\gamma = 2.37$. The values, $\vec{\theta}_{true}$, for the point source are the ones for NGC 1068: $\phi_0 = 5.0 \cdot 10^{-14}$ GeV^{-1} cm^{-2} s^{-1},

$E_0 = 1$ TeV and $\gamma = 3.2$. [5]
To not need to account for the atmospheric muon background, all events with $\cos(\theta) > 0$ (from IceCube's perspective) are cut. Therefore, the point source with the properties of NGC 1068 is set to a declination of 5° in this analysis.

5.3 Binned Poisson likelihood analysis

5.3.1 Binning

To reduce the computational cost, a binned instead of an unbinned analysis is used. In the diffuse-flux analysis the reconstructed muon energy is divided in 30 bins from 10^2 GeV to 10^8 GeV and the declination consists of 25 bins from $\sin(\delta) = 0$ to $\sin(\delta) = 1$.
In the point source analysis the same energy binning is used as in the diffuse-flux analysis. The second binning dimension is ψ^2, which is the squared angular difference between the true location of the source and the reconstructed event direction. Here $\psi = 3°$. [5] [22]

5.3.2 Expected event rates

The number of expected neutrinos for a diffuse flux is given by (from [22]):

$$N_\nu = T_{live} \int_{\Delta\Omega} d\Omega \int_{E_{min}}^{E_{max}} dE_\nu \; A_{\text{eff}}(E_\nu, \delta) \cdot \frac{d\phi_\nu}{dE_\nu} \cdot R_{E_\mu}(E_\mu^{rec}, E_\nu)\,, \tag{5.2}$$

and for a point source (from [5]):

$$N_\nu = T_{live} \int_0^\infty dE_\nu \; A_{\text{eff}}(E_\nu, \delta) \cdot \frac{d\phi_\nu}{dE_\nu} \cdot R_{E_\mu}(E_\mu^{rec}, E_\nu) \cdot R_\Omega(\Omega^\nu, \Omega^{rec}, E_\nu)\,, \tag{5.3}$$

where T_{live} is the time, the detector observed the source, R_{E_μ} is the energy resolution function and R_Ω the angular resolution function from subsection 5.1. $\frac{d\phi_\nu}{dE_\nu}$ is the neutrino flux. A_{eff} is the effective area.
In PLEnuM the effective area is obtained from the 10-year IceCube data release, [21]. However, in this study, it is calculated as described in section 4.

The integral formulations of the expected number of events are converted into a number of events per bin because a binned analysis is performed. The total number of events per bin is a sum of the events of background and signal:

$$\mu_{ij}(\vec{\theta}) = \mu_{ij}^{ast}(\vec{\theta}_{ast}) + \mu_{ij}^{atm}(\phi_0^{atm})\,, \tag{5.4}$$

where $\mu_{ij}(\vec{\theta})$ are the expected counts in each bin given the model parameters $\vec{\theta}$, which are as in subsection 5.2 for the background ϕ_0^{atm} and for the signal+background ϕ_0^{atm}, ϕ_0^{ast} and γ.
The Asimov data is created by setting the free model parameters in Equation 5.4 to the values described in subsection 5.2. Therefore, $n_{ij} = \mu_{ij}(\vec{\theta}_{true})$ [5].

5.3.3 Likelihood analysis

To obtain a detection significance in the end, a binned Poisson maximum likelihood analysis is used to fit the flux models. For each bin the expected event rates are compared to the Asimov data set. The likelihood function is:

$$\mathcal{L}(\vec{\theta}, n_{ij}) = \prod_{i,j} \frac{\mu_{ij}(\vec{\theta})^{n_{ij}}}{n_{ij}!} \cdot e^{-\mu_{ij}(\vec{\theta})} , \tag{5.5}$$

where $\mu_{ij}(\vec{\theta})$ are the expected counts in each bin given the model parameters $\vec{\theta}$ and n_{ij} are the Asimov data. With this formula, the best fit values of the model parameters can be obtained by maximization, or in practice, by minimizing the negative log-likelihood function. [5]

5.4 Hypothesis testing

To evaluate with which significance the background-only hypothesis can be rejected, a likelihood-ratio test is performed. The test statistic is defined as:

$$TS = -2\log\left(\frac{\mathcal{L}(H_0)}{\mathcal{L}(H_1)}\right) , \tag{5.6}$$

with $H_0 = \mu_{ij}(\phi_0^{atm})$ being the background hypothesis and $H_1 = \mu_{ij}(\phi_0^{atm}, \phi_0^{ast}, \gamma)$ being the signal hypothesis.
It is assumed that the sample size is large enough to apply Wilks' theorem, because of which the test statistic is assumed to approximately follow a χ^2-distribution under H_0. The p-value, p, is now determined by the integral of the χ^2-distribution starting from the value of the test statistic to infinity [6]. It is converted to a significance level, Z, by

$$Z = \Phi^{-1}(1-p) , \tag{5.7}$$

where Φ^{-1} is the cumulative distribution function of the unit Gaussian [23].

6 Comparison of different detector geometries

In section 4 the calculation and implementation of an effective area with detection efficiency, $\varepsilon \in [0,1]$, is introduced. Next, in section 5 the method of the likelihood analysis in the PLEnuM framework is described. For evaluating the significance with which the background-only hypothesis can be rejected for a certain diffuse or point source flux with a certain detector geometry and radius, both parts are combined into one analysis.
To do this, the effective area that was taken from the 10-year IceCube data release, [21], and was used in the PLEnuM analysis before, is replaced by the calculated effective area from section 4.
To include the detection efficiency in the effective area calculation, the detection efficiency matrices for the cylindrical and the "sunflower" geometry (see subsection 4.2) and the radii 500 m, 2000 m, 4000 m and 6000 m are precalculated, using 100 muons for the detection efficiency, and read in to be included in the effective area calculation and the subsequent likelihood analysis.

6.1 Realistic detector

6.1.1 Tested detector configurations

For the comparison of different detector geometries the following combinations were tested:

type of flux	diffuse, point source
geometry	cylinder, sunflower
detector radius	500 m, 2000 m, 4000 m, 6000 m
number of strings	91, 469, 1951
number of DOMs per string	25, 60, 75

The detector height was set to 1000 m for all configurations. The choice of the cylindrical and sunflower geometry types was made in order to match the current IceCube geometry, and that of the planned IceCube-Gen2 [20].

The radii were chosen to match the layout of IceCube, which has approximately a radius of 500 m and future detectors, e.g. NEON [24] or HUNT [12], which are planned to have a volume of up to 30 km^3. This corresponds to a radius of about 3000 m. Current and future detectors have or will have a height of around 1000 m. By modeling detectors with radii up to 6000 m, the behavior of even larger detectors is studied.

Since the detection efficiencies of the cylinder and sunflower geometries are compared, the same number of strings must be used. Because of the way the cylindrical geometry is implemented, only $1 + \sum_{i=1} i \cdot 6$ strings are possible, where i is the number of concentric rings of the cylindrical geometry. To get near the value of 86 strings of the current IceCube detector, $i = 5$ was chosen, which corresponds to 91 strings. The other numbers of strings were chosen similarly, but to come close to the values 500 and 2000.

The number of DOMs per string is tuned to model existing detectors, like IceCube with 60 DOMs per string, or future detectors, like NEON with about 25 DOMs per string [24], and 75 DOMs per string to investigate the effect of more DOMs.

When either performing a diffuse-flux or point source analysis, while leaving the height and number of DOMs per string constant, it is possible to compare different configurations:

- Compare the two geometries while leaving the string number and radius constant. This means that the string density is constant.
- Look, how different string numbers affect the significance while leaving the radius constant.
- Look at the effect of changing the radius and leaving string number and geometry the same.

6.1.2 Results and discussion

Diffuse-flux analysis

Overall, the results of the diffuse-flux analysis, shown in Figure 6.1, are consistent with the expectation that the detection significance increases with increasing number of strings, increasing number of DOMs per string and increasing radius. For example, the green curve in Figure 6.1 a) and the green and the blue curves in Figure 6.1 b) and c) are rising with increasing radius. Also, the significance values of the orange and the blue curves are increasing with more DOMs per string.
For a given radius and number of strings, the cylinder and the sunflower geometry have the same string density. Therefore, similar detection efficiencies for the cylindrical and the sunflower geometry for a certain string number and radius are expected and also observed in Figure 6.1. Because the sunflower geometry is chosen as layout for the future IceCube-Gen2 detector, it is also expected that the sunflower geometry performs better than the cylindrical geometry [20].

However, there are anomalies that do not match the expectations:

1. Some curves are not only rising, but also decreasing after a maximum.
   (e.g. orange and blue curve in Figure 6.1 a), orange curve in Figure 6.1 b) and c)).
2. The significance does not necessarily increase with a larger number of strings. For example in Figure 6.1 a), b) and c), the significance at a radius of 2000 m for the green configuration is lower than that of the blue configuration. In Figure 6.1 b) and c), this is also the case for the radius of 4000 m.

3. The significance does not always increase with more DOMs per string.
   The most prominent example for this anomaly are the values at a radius of 6000 m in Figure 6.1 a), b) and c). Here, the significance is actually decreasing. The significance in Figure 6.1 a) was probably that high, so that it was not possible to calculate it because of numerical issues.

4. The sunflower geometry does not always yield higher significance values than the cylindrical geometry.
   One example for this anomaly is the comparison of sunflower and cylinder geometry in Figure 6.1 c) for 1951 strings and a radius of 6000 m.

The first effect can be explained by the changing string density. A larger detector radius increases the detector volume. This causes, that the length, the muons travel in the detector gets larger, more DOMs can collect more photons and less events get filtered by the thresholds as described in subsection 4.2. This leads to a higher detection efficiency, therefore a larger effective area and also a larger significance. However, if the spacing gets too large, so that the DOMs detect less photons because the distance between the muon track and the DOMs gets large on average, less photons are detected by the DOMs (after Equation 4.3). Therefore, more events are filtered out and the significance decreases again.
The rise and the following decrease of the detection significance indicates that there is an optimal string density/spacing, which can be determined in future analyses by running more points.

The second effect might be caused by statistical fluctuations in the detection efficiency matrices (see subsection 4.2). There, only 100 muons were used for the calculation of one detection efficiency bin. With this low statistic, it is possible that the resulting effective area has a different value than it should have. This could then lead to anomalies like these, where some significance values for geometries with a larger number of strings are lower than the ones for geometries with less strings.

The third and fourth issue may also be caused by the low muon statistics in the calculation of the detection efficiency.

One additional effect is that at a radius of 500 m the significance does not increase with increasing string and DOM number and saturates at around 3.4σ. This means that beyond a certain instrumentation density, increasing the density even further does not improve the significance any more.

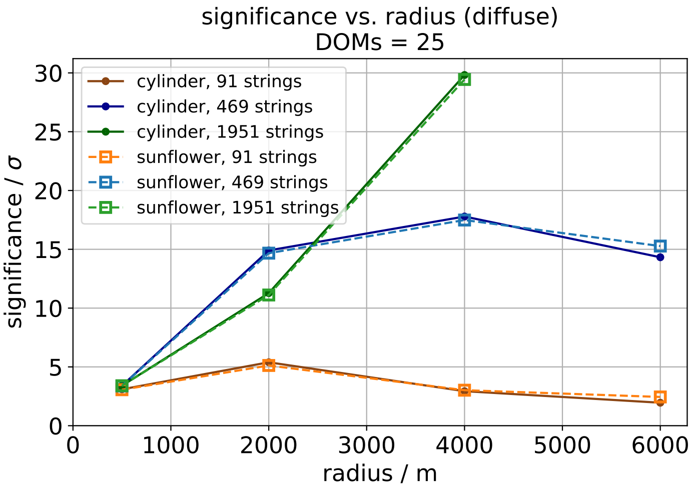

(a) DOMs per string = 25

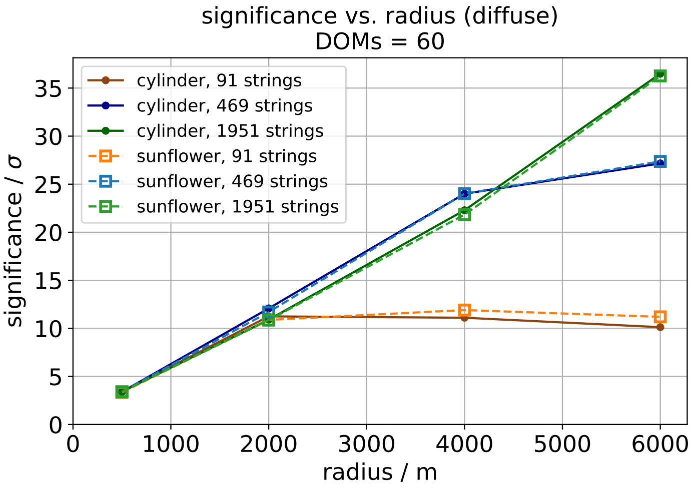

(b) DOMs per string = 60

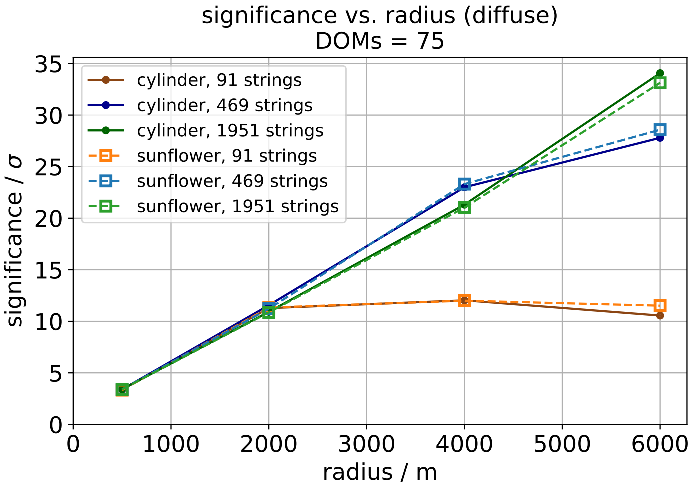

(c) DOMs per string = 75

Figure 6.1: Diffuse-flux analysis with a livetime of 1 yr and a spectral index $\gamma = 2.37$, using 100 muons for the calculation of the detection efficiency. The different detector geometries and string numbers are shown together in one plot. In the three plots the DOM number per string is changed.

Point source analysis

For the results of the point source analysis, shown in Figure 6.2, the same trends as in the diffuse-flux analysis are expected, i.e. the significance should increase with increasing number of strings, number of DOMs per string and radius. Also similar values for the significance of the sunflower and the cylindrical geometry are expected, but with the significances of the sunflower geometry being higher. For example, the green curves in Figure 6.2 b) and c) are rising with increasing radius.
In contrast to the diffuse-flux analysis the significance in the point source analysis here is always increasing with an increasing number of strings, which meets the expectations. For an increasing number of DOMs per string the significance increases most of the time. Only for the cylinder geometry with 1951 strings and a radius of 500 m, it is decreasing very slightly from 3.02σ for 25 DOMs per string to 3.00σ for 75 DOMs per string, and for 469 strings with a radius of 500 m from 2.96σ to 2.93σ.

However, there are still anomalies:

1. There are curves where the significance is decreasing with increasing radii.
   Examples are the blue and orange curves in Figure 6.2 a) and the orange curves in Figure 6.2 b) and c).
2. In Figure 6.2 b) and c) negative significance values occur.
3. The sunflower geometry does not always yield higher significances than the cylindrical geometry.
   One example for this issue are the green curves in Figure 6.2 b).

The reason for the first issue is, like in the diffuse-flux analysis, the decreasing string density for increasing radii at a constant number of strings. The optimal instrumentation density can be determined in future analyses by calculating more significance points.

The second anomaly arises from how the significance is calculated in PLEnuM. If the livetime of the detector in the analysis is too small, the PLEnuM analysis code produces a negative significance. When choosing a high-enough livetime, the analysis yields positive significance values. Here, the livetime of 1 yr was chosen, because a higher livetime would, for this configuration, cause numerical issues and produces an infinite value for the significance.

For the third problem the reasons might again be, like in the diffuse-flux analysis, the low muon statistics.

Like in the diffuse-flux analysis, a saturation effect at 500 m, for 60 and 75 DOMs per string is visible. There is only a small increase, from 2.6σ to 2.9σ, for larger string and DOM numbers. Also here, increasing the density beyond a certain instrumentation density, does not improve the significance any more.

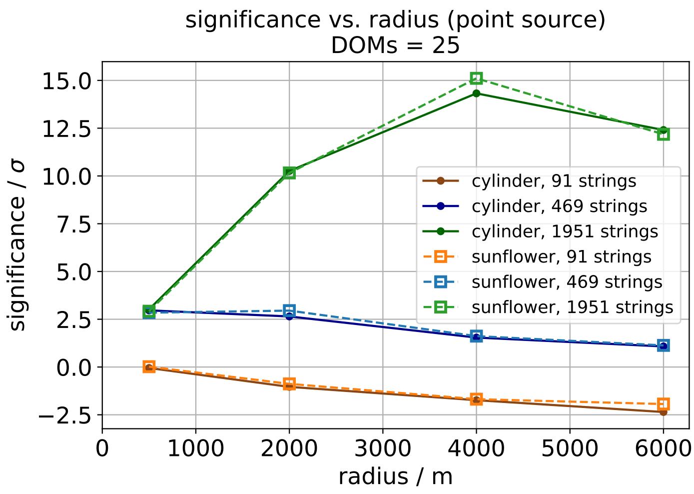

(a) DOMs per string = 25

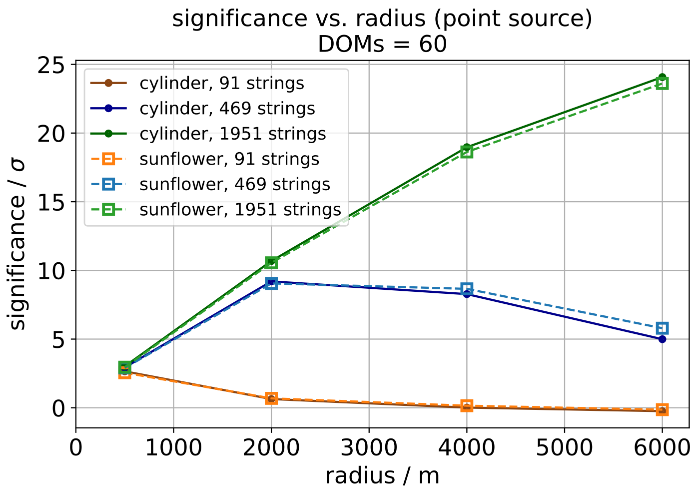

(b) DOMs per string = 60

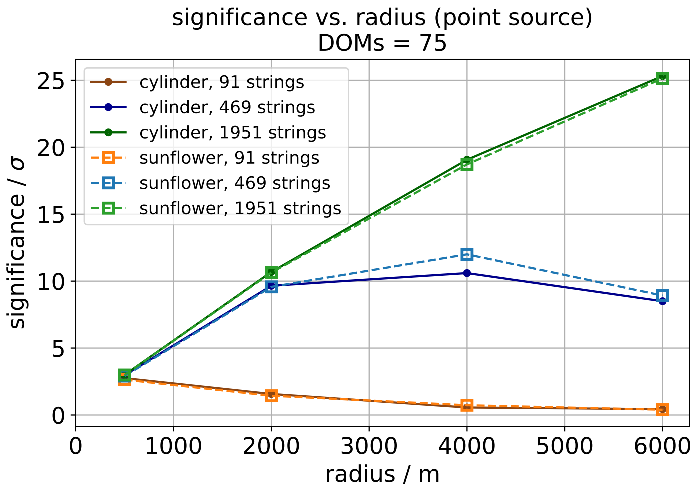

(c) DOMs per string = 75

Figure 6.2: Point source analysis with a livetime of 1 yr, a spectral index $\gamma = 3.2$ and a declination at 5°, using 100 muons for the calculation of the detection efficiency. The different detector geometries and string numbers are shown together in one plot. In the three plots the DOM number per string is changed.

Geometries yielding the best significance values

Based on the results obtained in the diffuse-flux analysis, the detector that yields the highest significance, is the cylindrical detector with 1951 strings, 60 DOMs per string and a radius of 6000 m (cf. Figure 6.1 b)). The calculated significance lies here at 36.5σ.
This is not the expected result, which would have been the sunflower detector with 1951 strings, 75 DOMs per string and a radius of 6000 m.
It is also obtained, that current detectors like IceCube with a radius of roughly 500 m, a height of 1000 m and a number of strings in the order of 100, have a good string density for detecting muon tracks that are produced on the surface of the detector, since increasing the string density does not increase the significance in this analysis (Figure 6.1 b)).

The result for the best detector in the point source analysis is closer to the expectation. The detector yielding the highest significance of 25.3σ was the cylindrical geometry with 1951 strings, 75 DOMs per string and a radius of 6000 m (cf. Figure 6.2 c)). The significance of the sunflower detector is with 25.1σ slightly smaller.
Like in the diffuse-flux analysis, the performance of current existing detectors for the detection of point sources would not increase notably with a denser string spacing.

However, due to the anomalies mentioned, the analysis should be refined and improved in the future, to be able to make correct and clear statements about the discovery performance of the tested detector geometries.

6.2 Comparison of a perfect and a realistic detector

Performing an analysis in which the detection efficiency is set to 1, yields incorrect results for the significance with which the background-only hypothesis is rejected. In this case, the effective area is overrated to some extent. However, in this section one example for a comparison between a perfect detector ($\varepsilon = 1$) and a more realistic detector ($\varepsilon \in [0, 1]$), as implemented in section 4, is done.

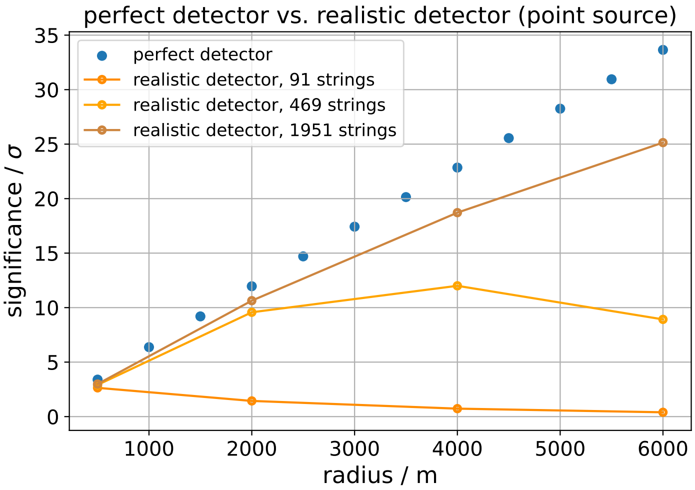

Figure 6.3: Comparison of the detection significance scaling of a perfect detector ($\varepsilon = 1$), as described in subsection 4.1, and a more realistic detector ($\varepsilon \in [0, 1]$). The comparison is done for a point source analysis with a cylindrical detector with 75 DOMs per string and a livetime of 1 yr (Figure 6.2 c)).

Comparing the perfect and the more realistic detector yields that the in the point source analysis result observed saturation effect at 500 m at 2.9σ, is close to the value of the perfect detector of 3.4σ. This means that with enough strings, every muon, generated on the detector surface, is detected.

The string density at the radius of 500 m is $1.16{\cdot}10^{-4}\ \frac{\text{DOMs}}{m^2}$ for 91 strings, $5.97{\cdot}10^{-4}\ \frac{\text{DOMs}}{m^2}$ for 469 strings and $2.48{\cdot}10^{-3}\ \frac{\text{DOMs}}{m^2}$ for 1951 strings.

Additionally, the larger the radius and the more strings the detector has, the closer its curve to the almost linearly rising curve of the ideal detector (cf. Figure 6.3 curve of the configuration with 1951 strings).

7 Outlook

This section gives an overview of possible further improvements and extensions to the implemented analysis that go beyond the scope of this thesis.

As described in subsubsection 6.1.1, some anomalies, like a decrease of the detection efficiency with more DOMs per string or more strings, occurred. The reason for these inconsistencies should still be found. One possible solution is the increase of the number of generated muons for the calculation of the detection significance (subsection 4.2). An error propagation through the whole analysis could also help in identifying if statistical fluctuations cause the anomalies. A calculation of detection efficiency matrices with 1000 muons per bin was already carried out. But the analysis was not performed yet, because of time constraints.

The analysis, though aiming for general detector optimization, is still based on some parameters that are only applicable to IceCube. This includes the detector resolution matrices from subsection 5.1, the usage of $\sin(\delta)$ = -$\cos(\theta)$, using the absorption-, scattering-length and Cherenkov angle of ice in Equation 4.3, the effective photon collection area of IceCube-DOMs and the modeling of the filter thresholds with the muon effective areas of IceCube in subsection 4.2. For a general detector optimization approach this needs to be generalized, and options for switching between water and ice models need to be implemented.

Additionally, these analyses are performed for only one specific diffuse- and one specific point source flux (see subsection 5.2). For an analysis that is able to compare between different models, e.g. different spectral indices, the calculation of the source discovery potential must be implemented. The discovery potential is the flux a point source needs to have on average, so that the background-only hypothesis can be rejected with a certain significance value, usually 5σ [5].

Currently, the muons that are generated to calculate the detection efficiency are produced uniformly on the surface of the detector. If in the future also muons outside of the detector are generated, their energy loss from their production point to the detector needs to be implemented.

When trying to identify a better detector geometry, more detector geometries need to be implemented for comparison and also more radii need to be included in the calculation to be able to fit the scaling of the significance, try to estimate a general behavior and to find the optimal string density.

Finally, in this thesis only muon neutrinos and therefore track-like events were considered. In the future, shower-like events should be included in order to perform an all-flavor optimization of detector geometries.

8 Summary and Conclusion

In this thesis, first steps in the development of a more computationally efficient method for determining optimized detector geometries for water/ice Cherenkov neutrino telescopes were taken.

First, a cylindrical and a sunflower detector geometry were introduced. Next, the effective area was calculated from neutrino, muon and detector properties, without using Monte Carlo simulations. Furthermore, to model non-perfect detectors, a detection efficiency $\varepsilon \in [0,1]$ was included in the effective area calculation. The detection efficiency was implemented by simulating muons in the detector, computing the light yield at the DOMs and applying filter thresholds that match the muon effective areas of IceCube (see subsection 4.2).

The calculated effective areas were then used in diffuse-flux and point source analyses, performed using an Asimov dataset and a likelihood optimization as implemented in the PLEnuM framework (see section 5). With this, the impact of different detector geometries on the detection significance was investigated. For the comparison of different detector geometries and configurations, various combinations of type of flux, geometry, detector radius, number of strings and DOMs per string are used (see subsubsection 6.1.1).

Overall, the results of both analyses are in general consistent with the expectation that the detection significance increases with increasing number of strings, increasing number of DOMs per string and increasing detector radius. Additionally, the sunflower geometry was expected to perform better than the cylindrical geometry. However, deviations from these expectations were found. They may result from a low muon statistic of only 100 muons in the calculation of the detection efficiencies.
It was observed that there is an optimal string density for a given number of strings and DOM number per string with varying radius. Also, when keeping the radius constant and increasing the density, there is an optimal density, beyond which the significance does not increase any more.

Due to the observed anomalies, the current analysis cannot quite be used for detector optimization yet. Nevertheless, it is an important first step in the development of a less computationally expensive optimization tool.

References

[1] Roberto Aloisio, Eugenio Coccia, and Francesco Vissani, eds. *Multiple Messengers and Challenges in Astroparticle Physics*. Cham, 2018. ISBN: 978-3-319-65423-2 978-3-319-65425-6. DOI: 10.1007/978-3-319-65425-6.

[2] R. Abbasi, M. Ackermann, J. Adams, et al. "Evidence for neutrino emission from the nearby active galaxy NGC 1068". In: *Science* 378.6619 (Nov. 4, 2022). ISSN: 0036-8075, 1095-9203. DOI: 10.1126/science.abg3395. arXiv: 2211.09972.

[3] IceCube et al. "Multi-messenger observations of a flaring blazar coincident with high-energy neutrino IceCube-170922A". In: *Science* 361.6398 (July 12, 2018). ISSN: 0036-8075, 1095-9203. DOI: 10.1126/science.aat1378. arXiv: 1807.08816.

[4] R. Abbasi, M. Ackermann, J. Adams, et al. "Observation of high-energy neutrinos from the Galactic plane". In: *Science* 380.6652 (June 30, 2023). ISSN: 0036-8075, 1095-9203. DOI: 10.1126/science.adc9818. arXiv: 2307.04427.

[5] Lisa Johanna Schumacher et al. *Beyond first light: global monitoring for high-energy neutrino astronomy*. Mar. 10, 2025. DOI: 10.48550/arXiv.2503.07549. arXiv: 2503.07549.

[6] Lisa Johanna Schumacher. PLEnuM: https://github.com/PLEnuM-group/Plenum.

[7] Christian Haack, Lisa Johanna Schumacher, and P-ONE Collaboration. "Machine-learning aided detector optimization of the Pacific Ocean Neutrino Experiment". In: *PoS*. 38th International Cosmic Ray Conference. Vol. ICRC2023. Nagoya, Japan, July 25, 2023, p. 1059. DOI: 10.22323/1.444.1059.

[8] Max Aker, Dominic Batzler, Armen Beglarian, et al. "Direct neutrino-mass measurement based on 259 days of KATRIN data". In: *Science* 388.6743 (Apr. 11, 2025). ISSN: 0036-8075, 1095-9203. DOI: 10.1126/science.adq9592. arXiv: 2406.13516.

[9] IceCube Collaboration et al. "Evidence for High-Energy Extraterrestrial Neutrinos at the IceCube Detector". In: *Science* 342.6161 (Nov. 22, 2013), p. 1242856. ISSN: 0036-8075, 1095-9203. DOI: 10.1126/science.1242856. arXiv: 1311.5238.

[10] Gisela Anton. *Neutrino Telescopes*. 2020. DOI: 10.1142/9789813275027_0002. arXiv: 2010.06012.

[11] R. Abbasi et al. "Improved Characterization of the Astrophysical Muon-Neutrino Flux with 9.5 Years of IceCube Data". In: *The Astrophysical Journal* 928.1 (Mar. 25, 2022), p. 50. ISSN: 0004-637X, 1538-4357. DOI: 10.3847/1538-4357/ac4d29. arXiv: 2111.10299.

[12] Tian-Qi Huang et al. "Proposal for the High Energy Neutrino Telescope". In: *PoS*. 38th International Cosmic Ray Conference. Vol. ICRC2023. Nagoya, Japan, Aug. 5, 2023, p. 1080. DOI: 10.22323/1.444.1080.

[13] IceCube Collaboration et al. “The IceCube Neutrino Observatory: Instrumentation and Online Systems”. In: *Journal of Instrumentation* 12.3 (Mar. 14, 2017). ISSN: 1748-0221. DOI: 10.1088/1748-0221/12/03/P03012. arXiv: 1612.05093.

[14] S. Adrián-Martínez et al. “Letter of Intent for KM3NeT 2.0”. In: *Journal of Physics G: Nuclear and Particle Physics* 43.8 (June 23, 2016), p. 084001. ISSN: 0954-3899, 1361-6471. DOI: 10.1088/0954-3899/43/8/084001. arXiv: 1601.07459.

[15] Baikal-GVD Collaboration et al. “Neutrino Telescope in Lake Baikal: Present and Future”. In: ICRC2019 (2020), p. 1011. DOI: 10.22323/1.358.1011. arXiv: 1908.05427.

[16] Leif Christian Rädel. “Measurement of High-Energy Muon Neutrinos with the IceCube Neutrino Observatory”. PhD thesis. Aachen: RWTH Aachen University, 2017.

[17] Christian Haack. *Personal Correspondence,* 2025.

[18] IceCube Collaboration et al. “Energy Reconstruction Methods in the IceCube Neutrino Telescope”. In: *Journal of Instrumentation* 9.3 (Mar. 17, 2014). ISSN: 1748-0221. DOI: 10.1088/1748-0221/9/03/P03009. arXiv: 1311.4767.

[19] Benedikt Mayer. Git repository for ToyCube simulation and neural network training: https://git.ecap.work/ob70ifit/toycube. 2025.

[20] Anastasiia Omeliukh et al. “Optimization of the optical array geometry for IceCube-Gen2”. In: *PoS.* 37th International Cosmic Ray Conference. Vol. ICRC2021. Berlin, Germany - Online, 2021, p. 1184. DOI: 10.22323/1.395.1184. arXiv: 2107.08527.

[21] IceCube Collaboration. *All-sky point-source IceCube data: years 2008–2018.* 2021. DOI: 10.21234/sxvs-mt83.

[22] Lisa Johanna Schumacher et al. “PLEnuM: A global and distributed monitoring system of high-energy astrophysical neutrinos”. In: *PoS.* Vol. ICRC2021. 2021, p. 1185. DOI: 10.22323/1.395.1185. arXiv: 2107.13534.

[23] O. Behnke et al. *Data Analysis in High Energy Physics: A Practical Guide to Statistical Methods.* Weinheim, 2013. ISBN: 978-3-527-41058-3.

[24] Huiming Zhang et al. “A proposed deep sea Neutrino Observatory in the Nanhai”. In: *Astroparticle Physics* 171 (May 13, 2025), p. 103123. ISSN: 09276505. DOI: 10.1016/j.astropartphys.2025.103123. arXiv: 2408.05122.

Acknowledgments

I'd like to thank my supervisors Lisa, Christian, and Claudio for their guidance and support throughout this thesis. A big thank you also goes to the members of my office and the IceCube group, the neutrino group, and ECAP - not only for proofreading my thesis and the support, but also for the many enjoyable lunches, coffee breaks, and free time activities.

Declaration of Originality

I, Elena Meier, student registration number: 22968471, hereby confirm that I completed the submitted work independently and without the unauthorized assistance of third parties and without the use of undisclosed and, in particular, unauthorized aids. This work has not been previously submitted in its current form or in a similar form to any other examination authorities and has not been accepted as part of an examination by any other examination authority.

Where the wording has been taken from other people's work or ideas, this has been properly acknowledged and referenced. This also applies to drawings, sketches, diagrams and sources from the Internet.

In particular, I am aware that the use of artificial intelligence is forbidden unless its use an aid has been expressly permitted by the examiner. This applies in particular to chatbots (especially ChatGPT) and such programs in general that can complete the tasks of the examination or parts thereof on my behalf.

Any infringements of the above rules constitute fraud or attempted fraud and shall lead to the examination being graded “fail” (“nicht bestanden”).

Place, Date

Signature